Forecasting Tropical Annual Maximum Wet-Bulb Temperatures Months in Advance from the Current State of El Niño

Yi Zhang[1,2], William R. Boos[1,3], Isaac Held[4], Christopher J. Paciorek[5], Stephan Fueglistaler[4,6]

[1]Department of Earth and Planetary Science, University of California, Berkeley, CA 94720
[2]Miller Institute for Basic Research in Science, University of California, Berkeley, CA 94720
[3]Climate and Ecosystem Sciences Division, Lawrence Berkeley National Laboratory, CA 94720
[4]Program in Atmospheric and Oceanic Sciences, Princeton University, Princeton, NJ 08540
[5]Department of Statistics, University of California, Berkeley, CA 94720
[6]Department of Geosciences, Princeton University, Princeton, NJ 08540

Key Points:

- Tropical wet-bulb temperatures (TW_{max}) peak around five months after El Niño winters.
- A multiple linear regression model considering the ENSO index and the long-term warming trend effectively explains TW_{max} variability.
- Our model quantifies the likelihood of strong El Niño and human-induced warming pushing TW_{max} to record-breaking levels.

Corresponding author: Yi Zhang, `yzhangaos@gmail.com`

Abstract

Humid heatwaves, characterized by high temperature and humidity combinations, challenge tropical societies. Extreme wet-bulb temperatures (TW) over tropical land are coupled to the warmest sea surface temperatures (SST) by atmospheric convection and wave dynamics. Here, we harness this coupling for seasonal forecasts of the annual maximum of daily maximum TW (TW_{max}). We develop a multiple linear regression model that explains 80% of variance in tropical mean TW_{max} and significant regional TW_{max} variances. The model considers warming trends and El Niño and Southern Oscillation (ENSO) indices. Looking ahead, a moderate-to-strong El Niño with an Oceanic Niño Index (ONI) of 1.5 by the end of 2023 suggests a 42% (11%, 78%) probability of breaking the tropical mean TW_{max} record in 2024. For an El Niño similar to 2015/2016 (ONI of 2.64), the probability escalates to 90% (50%, 99.5%). This approach also holds promise for regional TW_{max} predictions.

Plain Language Summary

The heat and humidity in the tropics can be particularly challenging for people to stay comfortable and healthy. This combination of heat and moisture is described using a measure called the wet-bulb temperature (TW). We found that these extremely humid and hot conditions on land can be predicted about five months in advance using a physics-based statistical model. The forecast is possible because the peak of El Niño comes before the peak in the warmest sea surface temperatures, which affects the maximum TW on land. This prediction can help tropical societies to better prepare for extreme heat.

1 Introduction

The tropics, characterized by high temperatures and humidities, face heightened risks from heat-related impacts (Sherwood & Huber, 2010; Raymond et al., 2020, 2021; Parkes et al., 2022). This vulnerability is exacerbated by the consistent warming trend, leading to more frequent and intense heat events. Superimposed on the warming trend is the El Niño-Southern Oscillation (ENSO). El Niño events, typified by warmer central and eastern equatorial Pacific Ocean temperatures, trigger shifts in atmospheric circulation that modify global temperature and precipitation patterns (Yulaeva & Wallace, 1994). These events often result in more frequent and intense heatwaves in many regions, including the tropics (Thirumalai et al., 2017; Arblaster & Alexander, 2012; Revadekar et al., 2009). In contrast, La Niña events, marked by cooler Pacific Ocean temperatures, tend to bring cooler and wetter conditions. In light of ongoing global warming, an El Niño event superimposed on the current warming could result in unparalleled hot weather, underscoring the need for further investigation and preparedness.

The physical mechanism underlying pan-tropical land warming during El Niño years is the free-tropospheric heating that arises from deep convection over anomalously warm SSTs. This heating causes atmospheric columns over remote land to adjust to a warmer state in response to the elevated free troposphere temperatures (Brown & Bretherton, 1997; Chiang & Sobel, 2002). Notably, this free-tropospheric warming occurs a few months after peak El Niños (Pan & Oort, 1983; Sobel et al., 2002; Chiang & Sobel, 2002), as the SSTs in convective regions (the warmer portions of tropical SSTs) take a few months to warm following peak El Niño events (Klein et al., 1999; Xie et al., 2009; Fueglistaler, 2019; Hogikyan et al., 2022).

As recognition of humid heat's importance grows, the effects of global warming and ENSO on extreme humid heat, in addition to extreme temperatures, are emerging as active areas of research. Anthropogenic warming is a primary driver of tropical increases in wet-bulb temperature (TW), a common measure of humid heat (Sherwood & Huber, 2010; Buzan & Huber, 2020; Zhang et al., 2021). According to Zhang et al. (2021), extreme TW in the tropics is projected to rise by 1°C for every 1°C increase in tropical mean warming due to the mechanism described above. Concurrently, ENSO variability can significantly impact TW patterns over shorter timeframes (Rogers et al., 2021; Speizer et al., 2022; Ivanovich et al., 2022). Research has highlighted anomalously high tropical land mean TW associated with the 1997-1998 El Niño (Raymond et al., 2020; Zhang et al., 2021), as well as the more frequent occurrence of regional extreme TW during El Niño years (Rogers et al., 2021; Speizer et al., 2022).

In this study, we draw upon existing knowledge that 1) maximum wet-bulb temperatures (TW_{max}) over land are influenced by the warmest sea surface temperatures (SSTs) in the tropics, and 2) a lag of about four months occurs in the warming of the warmest SSTs after a peak El Niño event. We aim to construct a predictive model for extreme TW that can provide early warning of extreme TW_{max} levels several months in advance. While earlier research has studied the delayed effects of El Niño the following summer in Asia, known as the "Indian Ocean capacitor effect" (Xie et al., 2009), our focus extends to extreme TW in all tropical land areas. Our research aims to enhance seasonal predictions of extreme TW in the tropics, offering more accurate climate risk assessments and enhancing preparedness efforts in these regions.

2 Data and Methods

2.1 Wet-bulb temperature

Wet-bulb temperatures (TW) are calculated using the ERA5 hourly reanalysis product (Hersbach et al., 2020) by solving the following equation:

$$c_p T_s + L_v q_s = c_p \mathrm{TW} + L_v q_{\mathrm{sat}}(\mathrm{TW}), \tag{1}$$

where T_s and q_s represent the 2-meter temperature and 2-meter specific humidity, respectively. L_v denotes the latent heat of vaporization, and c_p represents the specific heat capacity of air at constant pressure. In our computations, we use c_p as 1004.7090 J/kg/K and L_v as 2.5008$\times 10^3$ J/kg. Although neglecting the temperature dependence of c_p and L_v introduces a small error in TW, it is sufficient for our purposes.

Since the ERA5 dataset does not directly provide the 2-meter specific humidity, we calculate it using the hourly 2-meter dewpoint temperature (T_d) and surface pressure (p_s), considering the molecular mass ratio of water vapor and air (ϵ) of 0.621981. The specific humidity (q_s) is determined as follows:

$$q_s = \frac{\epsilon e_{\mathrm{sat}}(T_d)}{p_s - (1-\epsilon) e_{\mathrm{sat}}(T_d)}, \tag{2}$$

where e_{sat} represents the saturation vapor pressure calculated using the Clausius-Clapeyron equation, specifically the Teten's formula, consistent with the methodology of the European Centre for Medium-Range Weather Forecasts (ECMWF) (ECMWF, 2014):

$$e_{\mathrm{sat}} = a_1 e^{a_2 \frac{T-T_0}{T-a_3}}, \tag{3}$$

with the parameter values for saturation over water: a_1=611.21 Pa, a_2=17.502, a_3=32.19 K, and T_0=273.15 K.

To focus on extreme TW values, we consider the daily maximum TW and then determine the annual maximum, denoting it as $\mathrm{TW}_{\mathrm{max}}$.

2.2 ENSO index

The strength of the El Nino-Southern Oscillation (ENSO) phenomenon is assessed using the Oceanic Niño Index (ONI), which serves as NOAA's primary index for monitoring the oceanic component of ENSO. The ONI is calculated as the rolling 3-month average temperature anomaly, from the long-term average, of the surface of the east-central tropical Pacific near the International Dateline.

3 Results

3.1 ONI leads TW_{max} by months

To demonstrate that extreme TW over land is controlled by the warmest SSTs through the mediation of deep atmospheric convection and free-tropospheric wave dynamics, we show the time series of these variables in Figure 1a. All time series are presented as running means of 6 months with the monthly climatology removed. The tropical land-average of monthly maximum TW exhibits a notable long-term warming trend of approximately 0.2 K per decade from 1979 to 2022, accompanied by significant interannual variability. The monthly average 500-hPa temperature ($\overline{T_{500}}$) and the top 25% of monthly mean SST ($SST_{25\%}$) show similar interannual variabilities and long term trends as TW, with contemporaneous peaks. These findings support the notion put forward by Zhang et al. (2021) that the warmest SSTs control the maximum TW over land, with the coupling occurring rapidly enough to render the maximum TW and $SST_{25\%}$ variations appear nearly simultaneous in monthly data.

To predict extreme TW over land, we turn our attention to the predictors for the warmest 25% of SSTs. ENSO induces significant shifts in atmosphere-ocean circulations, altering the energy budget of the ocean's mixed layer and influencing the relatively warm SSTs that lie in regions of deep atmospheric convection. The interannual variability in $SST_{25\%}$ closely resembles that in the Oceanic Niño Index (ONI), which does not exhibit a long-term trend by design. Moreover, major El Niño events coincide with pronounced spikes in $SST_{25\%}$ and TW_{max} anomalies, with the latter two typically occurring with a lag of approximately four months. Notably, the warming of TW_{max} during the developing phase of the 1991-1992 El Niño was interrupted by the aerosol cooling effect of the Mt. Pinatubo eruption in June 1991, leading to a missed peak in TW_{max} despite rising ONI. Another significant volcanic eruption, El Chichón in 1982, also coincided with an

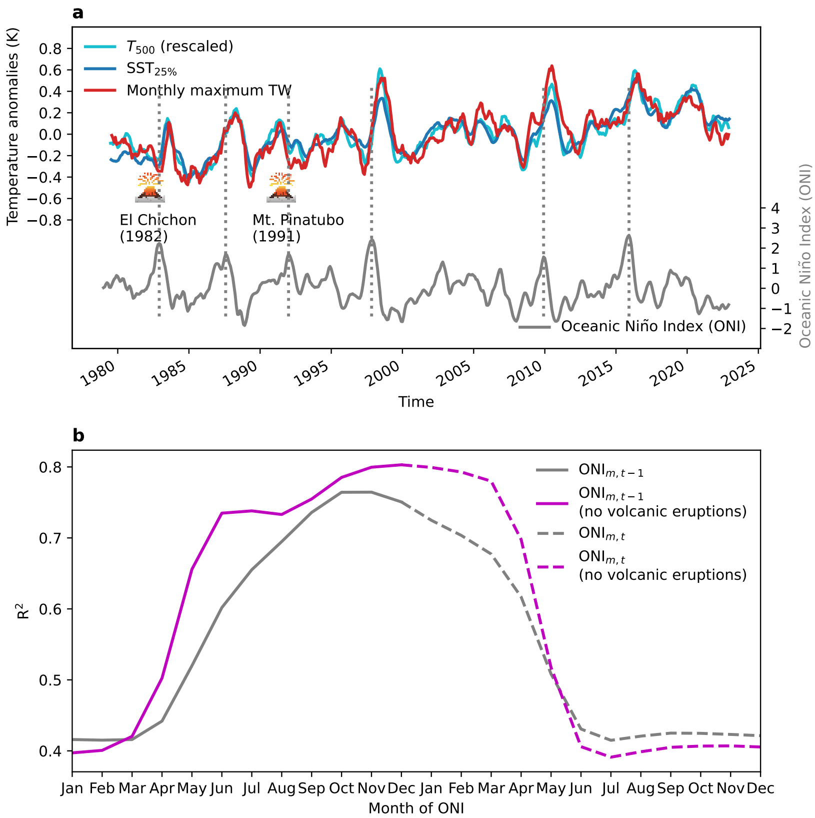

Figure 1. ENSO variability leads tropical land TW_{max} by a few months. **a**, Monthly anomalies of tropical (between 30°S and 30°N) land mean TW_{max} (red), the upper-quartile-mean SST (blue) from Hadley Centre Sea Ice and Sea Surface Temperature data set (HadISST) (Rayner et al., 2003), and the average 500-hPa temperature divided by the moist adiabatic amplification factor 1.4 (cyan), as well as the Oceanic Niño Index (ONI) in grey. Timing of strong El Niños (ONI >1.5) are marked with vertical dotted lines. **b**, R^2 values of the multiple linear regression model specified in Eq. (4) using ONI from January to December of preceding years (solid) and contemporaneous years (dashed). The grey line shows the fit using all 43 years between 1990 and 2022, while the magenta line shows the fit of 39 years to exclude major volcanic eruptions.

El Niño event. Although elevated TW_{max} values still occurred, they were partially offset by volcanic cooling, and the peak TW_{max} lagged the ONI peak by 9 months. Excluding the volcanic eruptions, other major El Niño events consistently precede anomalous high $SST_{25\%}$ values and, consequently, extreme TW_{max} values. These findings suggest the potential to use the ONI to statistically predict TW_{max} some months later, perhaps even in the following year.

3.2 Multiple linear regression model of TW_{max}

We develop a multiple linear regression model to predict the annual maximum of daily maximum wet-bulb temperature (TW_{max}) using two independent variables: a year variable to account for the warming trend and the Oceanic Niño index (ONI) to represent ENSO. The objective is to explain anomalies in TW_{max} as a linear combination of a constantly rising baseline and the ONI from a specific month of the preceding year:

$$\mathrm{TW}_{\max,t} = \beta_0 + \beta_1 t + \beta_2 \mathrm{ONI}_{m,t-1} + \epsilon_t \tag{4}$$

Initially, we examine whether this model can capture the tropical land average values of TW_{max} between 30°S and 30°N. Even though the exogenous variable is an annual maximum, the process of spatial averaging yields an error term with a near-Gaussian distribution, justifying the use of multiple linear regression analysis. We compute the R^2 values for different months (m) in the model using the tropical land average of TW_{max} from 1980 to 2022, with the year t and ONI from 1979 to 2021 as the independent variables (Figure 1b). The highest R^2 value of 0.764 is obtained when using the ONI from all Novembers to predict the land-mean TW_{max} in the following years. However, considering the impact of major volcanic eruptions on TW_{max}, we exclude the years affected by these eruptions to enhance the accuracy of the linear regression model. We exclude TW_{max} for the two years following the Mt. Pinatubo eruption (1992 and 1993) and the two years following the El Chichón eruption (1983 and 1984). Consequently, we discard ONI values from 1982, 1983, 1991, and 1992. The performance of the regression improves, with the highest R^2 value of 0.803 achieved using December ONI from the preceding year. Notably, the R^2 values exhibit substantial increases from April to August, reaching a relatively high value of 0.735 in June. This aligns with the spring predictability barrier and suggests that a skillful prediction for TW_{max} in the subsequent year might be obtained as early as June of the current year.

For completeness we also show the R^2 values using ONI for each month of the same year as the $\mathrm{TW_{max}}$ in Figure 1b. The explained variance does not increase when using ONI of the same year as the occurrence of $\mathrm{TW_{max}}$. This is because $\mathrm{TW_{max}}$ over land is not constrained by the contemporaneous ONI but rather the warmest SSTs which lag ONI by a few months.

Given the performance of December ONI (years affected by volcanic eruptions excluded), all regression in the rest of the paper are against December ONI with the four years affected by volcanism removed between 1980 and 2022, resulting in 39 data points and two independent variables. Note that the ONI is a three-month running mean, therefore December ONI values contain information from January of the following years; however, $\mathrm{TW_{max}}$ occurs in January primarily for some land regions south of 15°S (Figure S3), and we later demonstrate predictive skill of the model 3-7 months in advance for some sample regions.

Figure 2 illustrates the multiple linear regression model in Eq. (4) when m is December. There is negligible multicollinearity between the two independent variables (Figure 2a), year (t) and ONI of the preceding December ($\mathrm{ONI}_{\mathrm{Dec},t-1}$). Each independent variable alone explains slightly less than 40% of variance in the tropical mean $\mathrm{TW_{max}}$. Figure 2d shows the observed versus the model-predicted $\mathrm{TW_{max}}$ with 80% of variance explained.

3.3 Impact of warming trend and ENSO variability on $\mathrm{TW_{max}}$

To assess the relative contributions of warming and ENSO to explaining the variance in $\mathrm{TW_{max}}$, we estimate the standardized regression coefficients ($\hat{\beta}^*$) by carrying out the multiple linear regression on standardized variables, with the standardization following $\frac{x-\overline{x}}{s_x}$ where $\overline{x}$ denotes the average and s_x the standard deviation. The standardized regression coefficients provide the change in the dependent variable per one-unit change in the independent variable measured in standard deviations. The 95% confidence intervals of the standardized coefficients for the warming trend and ENSO variability are 0.65 ± 0.15 and 0.64 ± 0.15, indicating that both factors contribute similarly to the variance of the tropical land mean $\mathrm{TW_{max}}$ (Figure 3a).

To examine the spatial distribution of these coefficients, we compute $\hat{\beta}^*$ by regressing the standardized zonal land mean $\mathrm{TW_{max}}$ (i.e., $\mathrm{TW_{max}}$ at each grid point zonally

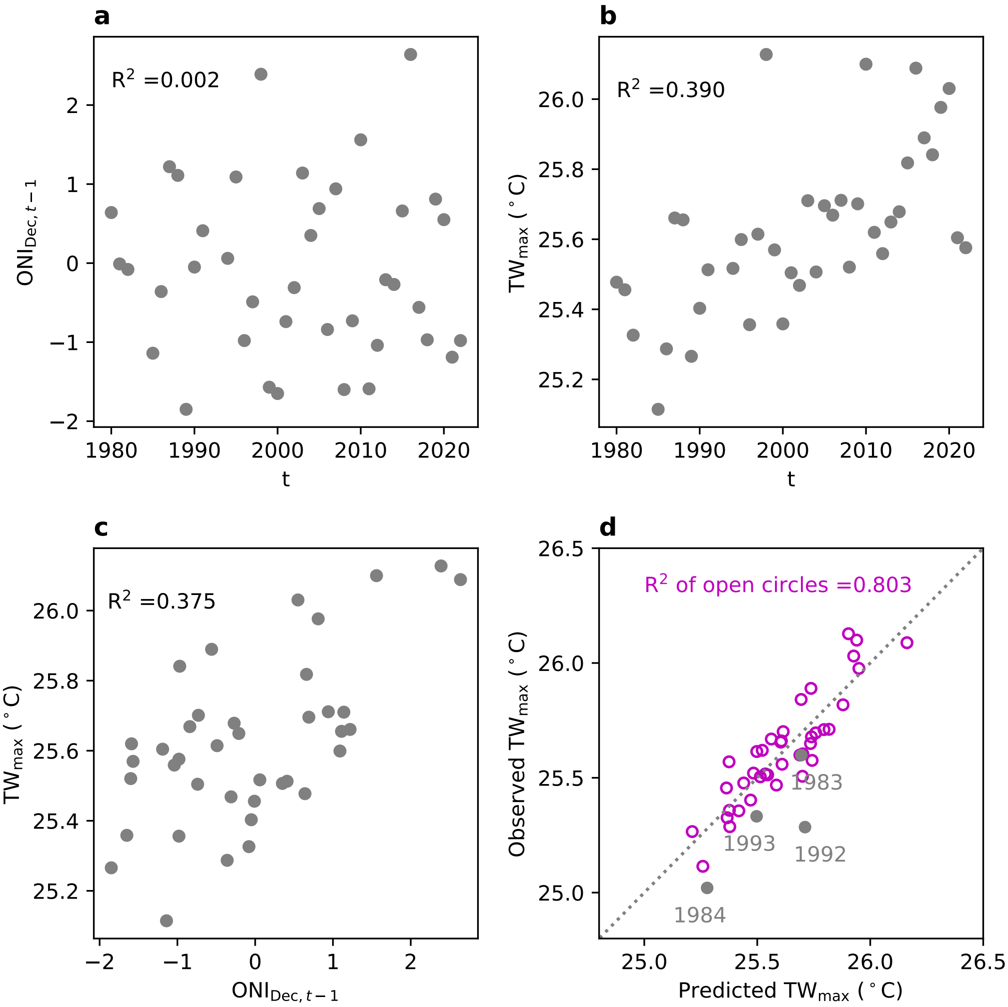

Figure 2. Visualization of the multiple linear regression for 30°S-30°N land-mean TW_{max}. **a**, Scatter plot of independent variables – December ONI of preceding years ($ONI_{Dec,t-1}$) and year (t). **b**, Scatter plot of 30°S-30°N land-mean TW_{max} and year (t). **c**, Scatter plot of 30°S-30°N land-mean TW_{max} and $ONI_{Dec,t-1}$. **d**, Actual TW_{max} from ERA5 versus the predicted TW_{max} by the regression model (open circles). Years following major volcanic eruptions are excluded from the fit and are plotted separately in grey. The grey dotted line indicates 1/1.

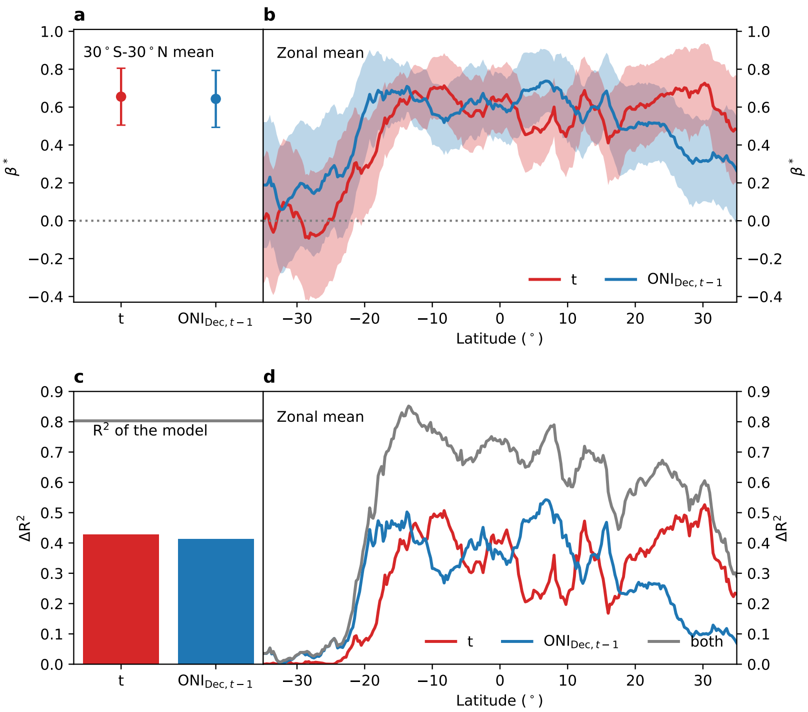

Figure 3. Relative importance of constant warming and ENSO variability in explaining TW_{max} variability. **a**, Standardized regression coefficients ($\hat{\beta}^*$) and the 95% confidence intervals for both independent variables. **b**, Same as **a** but for zonal mean TW_{max} over land. **c** and **d**, Incremental R^2 (ΔR^2) for each independent variable, estimated by removing each variable from the full regression, and the R^2 of the full model (grey).

averaged over land only) against the same two standardized independent variables. Figure 3b illustrates the estimated β^* as a function of latitude. Over most latitudes in the tropics, the 95% confidence intervals of $\hat{\beta}_1^*$ (warming) and $\hat{\beta}_2^*$ (ENSO) strongly overlap, suggesting a similar contribution at each latitude. However, in the southern subtropics, the magnitude of $\hat{\beta}^*$ values for both variables declines, and the 95% confidence interval encompasses 0 south of 20°S, indicating that the regression model is not valid in these latitudes. Notably, warming exerts a stronger influence on the northern subtropics compared to ENSO.

The implications of a one-standard-deviation change may differ when the independent variables follow the same type of distribution, as is the case here with the uniformly distributed t variable and the approximately normally distributed ONI. To provide further evidence and a complementary perspective, we employ an alternative approach by calculating the increment in R^2 (ΔR^2) for each variable:

$$\Delta R_i^2 = R_{\text{full}}^2 - R_{\text{Reduced},i}^2, \tag{5}$$

where R_{full}^2 represents the R^2 value of the full model (Eq. 4), and $R_{\text{Reduced},i}^2$ corresponds to the R^2 value when the ith independent variable is removed from the regression model. ΔR_i^2 can be loosely regarded as the contribution of the ith variable to the full model. This method yields similar results (Figure 3c,d), with warming contributing 0.428 and ENSO contributing 0.413 for the tropical mean TW_{max}. The latitudinal patterns of the relative magnitudes of ΔR^2 values closely resemble those of $\hat{\beta}^*$. Furthermore, the R^2 value of the full model indicates that the model performs best in the deep tropics, consistent with with empirical findings that support the validity of the weak-temperature-gradient assumption in that latitudinal range (Zhang & Fueglistaler, 2020).

3.4 Regional regression

When evaluating the model's performance for gridbox-level annual maxima, the assumption of a Gaussian error term in Eq. (4) becomes less appropriate. In this context, we assume a generalized extreme value (GEV) distribution for the error term and determine the parameters through maximum likelihood estimation (Text S1).

The model's performance exhibits a spatial pattern consistent with the zonal-mean analysis discussed above, with its lowest RMSE values in the deep tropics and an increase towards higher latitudes (Figure 4a).

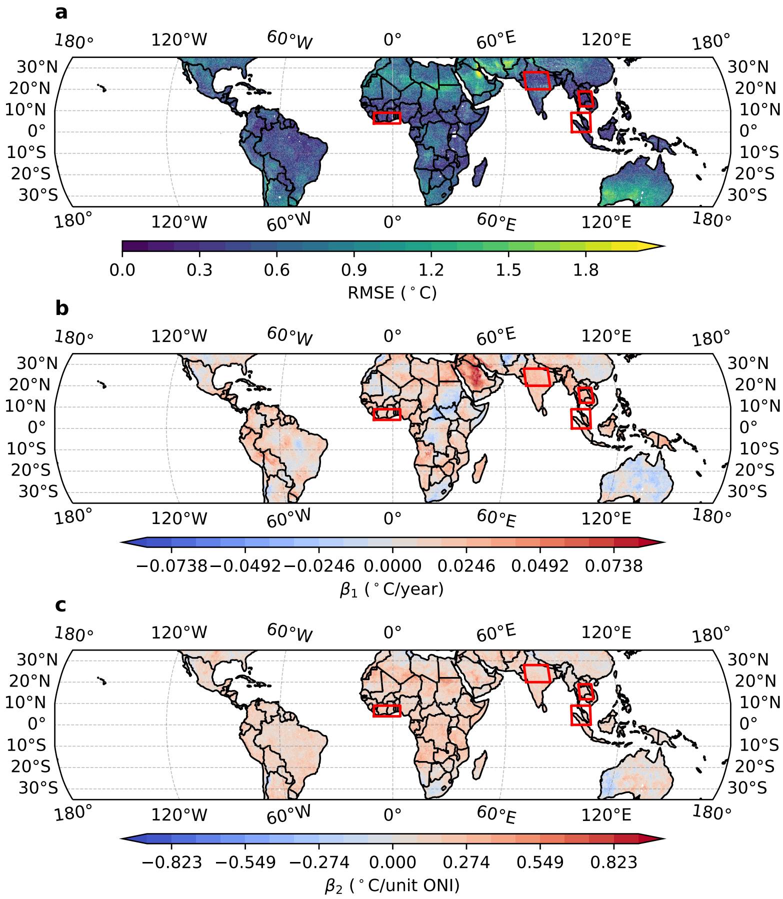

Figure 4. Results of fitting the model in Eq 4 at each location. **a**, R^2. Red boxes outline regions of interest further analyzed in Figure 5. **b**, Standardized regression coefficient of warming. **c**, Standardized regression coefficient of ENSO variability.

The $\hat{\beta}$ values for both warming (Figure 4b) and ENSO (Figure 4c) are comparable in magnitude when multiplied by the standard deviations of the respective independent variable, implying their similar impacts on $\mathrm{TW}_{\mathrm{max}}$ variability across different locations. Contrary to expectations that $\mathrm{TW}_{\mathrm{max}}$ in all tropical land is constrained by the warmest SSTs irrespective of place, the coefficient for warming ($\hat{\beta}_1$; Figure 4b) exhibits notable spatial variations. In contrast, the ENSO coefficient ($\hat{\beta}_2$; Figure 4c) is relatively uniform, with El Niños leading to higher $\mathrm{TW}_{\mathrm{max}}$ in the following years across most regions. This suggests that, despite El Niño's inherent spatial characteristics, its occurrence induces a relatively uniform response in the following year's continental $\mathrm{TW}_{\mathrm{max}}$.

There are two potential causes of the spatial pattern in the coefficient of warming ($\hat{\beta}_1$): the influence of local land surface conditions, and the uneven response of free-tropospheric temperatures to localized convective heating (Matsuno, 1966; Gill, 1980). Further analysis suggests that the former is more likely, as evidenced by the fact that the areas of negative $\hat{\beta}_1$ coincide with regions of strongly negative trends in the annual-mean 2-m specific humidity (q_s; Figure S1b). Such drying trends could stem from land use change, a process not explored in this study. A drier land surface deepens the planetary boundary layer, distributing surface heat fluxes within a deeper layer and enhancing entrainment of dry free tropospheric air; both of these processes lead to lower boundary layer moist static energy and surface TW (Pal & Eltahir, 2001; Kong & Huber, 2023).

The above analyses illustrate the spatial heterogeneity in the relationships of $\mathrm{TW}_{\mathrm{max}}$ with warming and ENSO. While it is reasonably true that tropical $\mathrm{TW}_{\mathrm{max}}$ increases over land are uniformly limited by the warmest sea surface temperatures (Zhang et al., 2021), the regional disparities highlight the limitation of this assumption. These results emphasize the importance of conducting localized assessments, which we do next.

We have chosen four regions (marked as red boxes in Figure 4a) to assess how the model in Eq. (4) predicts regional-mean $\mathrm{TW}_{\mathrm{max}}$. The choice of these regions is not governed by any strict rule, but we generally pick regions that exhibit relatively high values in climatological $\mathrm{TW}_{\mathrm{max}}$ (Figure S2a) and population density (Figure S2b), and relatively low values in RMSE (Figure 4a). Spatial averaging produces error terms approximating Gaussian distributions, justifying the suitability of applying the multiple linear regression analysis. The model's performance in these smaller regions is depicted in Figure 5b-d, while Figure 5a illustrates the same for the tropical land mean. The model ef-

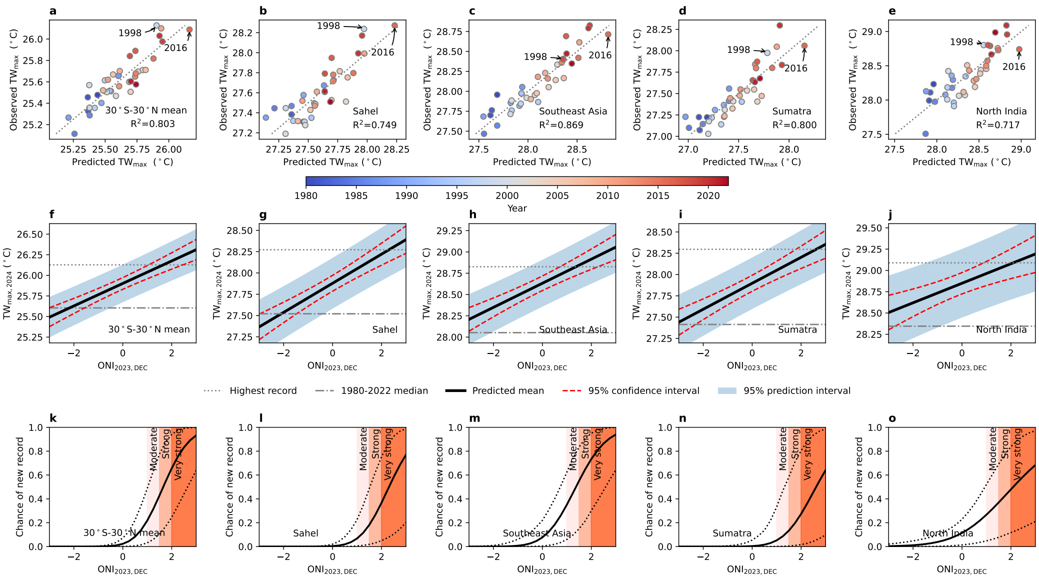

Figure 5. Example TW_{max} forecast for 2024. **a-e**, Performance of multiple linear regression for 30°S-30°N land mean and four regions marked in Figure 4a. Color indicates the year of the data point. Two major El Niños-1998 and 2016-are highlighted. **f-j**, Predicted $TW_{max,2024}$ as a function of December ONI, 2023. Confidence intervals in red account for the standard error of the predicted mean. Prediction intervals in blue additionally take into account the year-to-year variability around the predicted mean. **k-o**, Estimated chance of TW_{max} setting new records in 2024 in the tropical mean and each region conditioned upon the strength of El Niño by the end of 2023. ONI ranges of moderate ($1.0 \leq ONI < 1.5$), strong ($1.5 \leq ONI < 2.0$) and very strong ($ONI \geq 2.0$) El Niño events are marked.

Table 1. Summary of multiple linear regression results[a]

Region	30°S-30°N mean	Sahel	Southeast Asia	Sumatra	North India
$\hat{\beta}_1$ (°C/year)	0.0125±0.0029[b]	0.0121±0.0037	0.0235±0.0034	0.0184±0.0038	0.0218±0.0050
$\hat{\beta}_2$ (°C/unit ONI)	0.137±0.032	0.171±0.042	0.141±0.038	0.152±0.042	0.115±0.056
$\hat{\beta}_1^*$ (standardized $\hat{\beta}_1$)	0.65	0.55	0.84	0.73	0.78
$\hat{\beta}_2^*$ (standardized $\hat{\beta}_2$)	0.64	0.70	0.45	0.55	0.37
ΔR_1^2	0.428	0.300	0.700	0.538	0.607
ΔR_1^2	0.413	0.483	0.203	0.298	0.135
R^2	0.803	0.749	0.869	0.800	0.716
F-statistic, P>F	73.36, 2.0e-13	53.66, 1.6e-11	119.3, 1.3e-16	72.04, 2.6e-13	45.50, 1.4e-10
t, P> |t| for $\hat{\beta}_1$	8.844, 1.5e-10	6.557, 1.3e-07	13.859, 5,3e-16	9.843, 9.5e-12	8.783, 1.8e-10
t, P> |t| for $\hat{\beta}_2$	8.686, 2.3e-10	8.321, 6.6e-10	7.465, 8.1e-9	7.328, 1.2e-8	4.134, 2.0e-4
Root Mean squared error (RMSE; °C)[c]	0.103	0.134	0.124	0.136	0.182
Leave-one-out cross-validation RMSE (°C)	0.113(+9.45%[d])	0.147(+9.17%)	0.135(+8.86%)	0.149(+9.05%)	0.199(+9.71%)
Walk-forward validation RMSE (°C)	0.119(+7.08%[e])	0.138(+20.1%)	0.156(+17.6%)	0.171(+18.8%)	0.194(+17.6%)
Record-setting probability (ONI=1.5)	42%(11%-78%[f])	15%(1.8%-49%)	56%(15%-84%)	11%(0.5%-58%)	35%(7.7%-69%)
Record-setting probability (ONI=2.64)	90%(50%-99.5%)	66%(14%-95%)	92%(55%-99.5%)	51%(5.5%-95%)	63%(17%-94%)

[a] Number of Observations: 39; Residuals degree of freedom: 36; Model degree of freedom: 3

[b] 95% confidence interval

[c] Maximum likelihood estimate of MSE, not the unbiased MSE, is used throughout the paper

[d] Percentage change compared to the regression model with all 39 data points

[e] Percentage change of RMSE of the last 19 data points

[f] 95% BCa bootstrap interval

fectively explains TW_{max} variability at both regional and tropical mean scales. The contributions of warming and ENSO exhibit regional variations, as evidenced by the range of ΔR^2 values in Table 1. In Southeast Asia, for instance, the variability of TW_{max} is predominantly influenced by the warming trend, with higher TW_{max} values occurring in more recent years (Figure 5c). Conversely, the Sahel region exhibits stronger sensitivity to ENSO variability, with 1998 and 2016 having the highest TW_{max} (Figure 5b).

TW_{max} occur at different times of year in different regions. A general pattern emerges, with TW_{max} events occurring during boreal summer (June-August) north of 15°N, boreal winter (December-February) south of 15°S, and boreal spring (March-May) and fall (September-November) between 15°S and 15°N (Figure S3a). For the four selected regions, TW_{max} typically occurs in April for Sahel, May for Southeast Asia and Sumatra, and June to August for North India (Figure S3b). The multiple linear regression model thus demonstrates an average lead time of approximately five months for tropical land areas and a range of three to seven months for the four regions of interest.

3.5 Forecasting $\mathbf{TW_{max}}$ months in advance

Before making predictions with the multiple linear regression model, we assess its predictive skill using leave-one-out cross-validation and walk-forward validation which is more suitable for time series data. This is motivated by the possibility of overfitting, especially since our model was trained using the full dataset. The moderate increases in RMSE during cross-validation (Table 1) suggest that the model is not seriously overfitted and is suitable for making predictions with details provided in Text S2 and Figures S4.

Our objective is to generate a forecast of $\mathrm{TW_{max}}$ for the upcoming year based on the December Oceanic Niño Index (ONI) of the current year. Note that the ONI is a three-month running mean, with December ONI of the current year technically containing information from January of the upcoming year, but nearly all land north of 15°S has $\mathrm{TW_{max}}$ occurring in March or later of the upcoming year (Figure S3b). Taking the year 2024 as an example, the predicted mean depends on $\mathrm{ONI_{Dec,2023}}$ following:

$$\hat{\mathrm{TW}}_{\mathrm{max},2024} = \hat{\beta}_0 + 2024\hat{\beta}_1 + \hat{\beta}_2 \mathrm{ONI}_{\mathrm{Dec},2023}. \quad (6)$$

Figure 5e-h presents the 95% confidence intervals of the predicted mean and the 95% prediction intervals of $\mathrm{TW_{max,2024}}$ as a function of $\mathrm{ONI_{Dec,2023}}$ (Text S3). As expected, even in a neutral ENSO state, the mean predicted $\mathrm{TW_{max,2024}}$ values in all four regions (Figure 5f-h) as well as the tropical mean (Figure 5e) surpass the median of past records. This demonstrates the influence of the cumulative warming at the present level on $\mathrm{TW_{max}}$. A rough estimate of the impact of warming since 1980 on $\mathrm{TW_{max}}$ is the number of years (44 years) multiplied by $\hat{\beta}_1$, yielding 0.55 K for the tropical mean. The ONI value required to achieve a comparable effect can be estimated by dividing the warming-induced increase in $\mathrm{TW_{max}}$ by $\hat{\beta}_2$. Remarkably, an ONI value of 4.0, representing a super El Niño of unprecedented magnitude, would be necessary to match the increase in tropical mean $\mathrm{TW_{max}}$ caused by cumulative warming. Although this estimation is not rigorous, it provides an estimate of the magnitude of the cumulative warming effect since 1980, equivalent to an exceptionally strong El Niño.

Next, we estimate the probability of a new $\mathrm{TW_{max}}$ record being set in 2024, assuming knowledge of $\mathrm{ONI_{Dec,2023}}$. Rigorously estimating this probability is challenging, and our estimate is contingent upon certain assumptions. We assume that the predicted

$\mathrm{TW_{max}}$ at each $\mathbf{x_p} = (1, 2024, \mathrm{ONI_{Dec,2023}})^{\mathrm{T}}$ follows a Gaussian distribution centering at the predicted mean given by Equation (6) with a standard deviation equalling the root mean squared error (RMSE; we use the maximum likelihood estimate of RMSE rather than the unbiased estimate). For each $\mathrm{ONI_{Dec,2023}}$ value, we then compute the area under this Gaussian distribution when the predicted $\mathrm{TW_{max}}$ exceeds the highest record, resulting in the central estimates of the probability of a new $\mathrm{TW_{max}}$ record being set (solid lines in Figures 5i-l). The 95% confidence intervals for this probability, shown as dotted lines in Figures 5i-l, were derived using the bias-corrected and accelerated (BCa) bootstrap method (Text S4).

For the tropical mean $\mathrm{TW_{max}}$, an Oceanic Niño Index (ONI) of 1.5 by the end of 2023 leads to a central estimate of a 42% probability of surpassing the $\mathrm{TW_{max}}$ record in 2024 with the 95% confidence interval ranging from 11% to 78% (Figure 5k). In contrast, if an El Niño as intense as the 2015/2016 event (with an ONI of 2.64) occurs, the central probability estimate increases to 90%, with the 95% confidence interval ranging from 50% to 99.5% (Figure 5k). These probabilities as well as the width of the confidence intervals exhibit regional variability (Table 1), with Southeast Asia emerging as a region with an elevated likelihood of experiencing record-breaking $\mathrm{TW_{max}}$ during a strong El Niño (Figure 5m, Table 1).

4 Summary and Discussion

This study establishes the potential for dynamically based predictions of the annual maximum of daily maximum wet-bulb temperatures ($\mathrm{TW_{max}}$) across tropical land areas with an average lead time of five months. This predictability arises from two facts in tropical atmosphere-ocean dynamics: 1) $\mathrm{TW_{max}}$ over tropical land is closely coupled to free tropospheric temperature through deep convection and tropical wave dynamics, and 2) the free tropospheric temperature is determined by the warmest SSTs, which typically reach their peak around five months after the peak of an El Niño event (Pan & Oort, 1983; Sobel et al., 2002; Chiang & Sobel, 2002).

By using the Oceanic Niño Index (ONI) as a predictor and accounting for the warming trend through a “year” variable, our multiple linear regression model effectively explains a substantial portion—80%—of the variability in tropical land mean $\mathrm{TW_{max}}$. Although the model's performance varies across regions, it demonstrates promising skills, especially in the deep tropics (Figures 3b,d, Figure 4a). Both warming trends and ENSO have contributed significantly to the variability in $\mathrm{TW_{max}}$, and our analysis shows that the cumulative warming effect since 1980 is comparable to that of an exceptionally strong El Niño.

We forecasted $\mathrm{TW_{max}}$ for the year 2024 assuming knowledge of the December ONI of 2023 and estimated the probability of setting new $\mathrm{TW_{max}}$ records in 2024. The strength of an El Niño event significantly influences the probability of breaking $\mathrm{TW_{max}}$ records. The tropical mean and regional variations in these probabilities are detailed in Figure 5k-o and Table 1.

Although TW may not be the most precise metric for evaluating heat stress (Lu & Romps, 2023; Baldwin et al., 2023), the methodology developed in this work has the potential to be adapted to temperature and Heat Index, which are influenced by SST through similar dynamics (Chiang & Sobel, 2002; Byrne, 2021).

Finally, this study calls for increased efforts to enhance the accuracy of predictions of ENSO-induced free-tropospheric temperature variations. Improved predictions for free-tropospheric temperatures, such as T_{500}, could benefit projections of extreme heat stress across tropical continents, as illustrated by the close correlation between the two in Figure 1a. Note that the predictive model proposed in this study does not rely on forecasting future ENSO events; it leverages only the current ENSO state. This model's predictive skill originates from the time lag between tropical tropospheric temperatures and ENSO variability. That said, advances in ENSO forecasting could further extend the lead times at which accurate $\mathrm{TW_{max}}$ predictions become feasible.

Acknowledgments

Y.Z. acknowledges the support from the Miller Institute for Basic Research in Science at the University of California, Berkeley. This research was partially supported by the Director, Office of Science, Office of Biological and Environmental Research of the U.S. Department of Energy as part of the Regional and Global Model Analysis program area within the Earth and Environmental Systems Modeling Program under Contract No. DE-AC02-05CH11231 and used resources of the National Energy Research Scientific Computing Center (NERSC), also supported by the Office of Science of the U.S. Department of Energy, under Contract No. DE-AC02-05CH11231. The authors thank the Statistical Consulting provided by the Department of Statistics at the University of California Berkeley, represented by Hyunsuk Kim and James B. Brown, and Mark Risser for their valuable feedback on the statistical approaches.

Open Research

The Oceanic Niño Index (ONI) is provided by National Oceanic and Atmospheric Administration's Climate Prediction Center and is available here: `https://origin.cpc.ncep.noaa.gov/products/analysis_monitoring/ensostuff/ONI_v5.php`. The ERA5 hourly data on pressure levels and single levels from 1979 to present are downloaded from the Copernicus Climate Change Service Climate Data Store (`https://cds.climate.copernicus.eu`). The Hadley Centre Sea Ice and Sea Surface Temperature data set (HadISST) is downloaded from `https://www.metoffice.gov.uk/hadobs/hadisst/`.

References

Arblaster, J. M., & Alexander, L. V. (2012). The impact of the el niño-southern oscillation on maximum temperature extremes. *Geophysical Research Letters*, *39*(20).

Baldwin, J. W., Benmarhnia, T., Ebi, K. L., Jay, O., Lutsko, N. J., & Vanos, J. K. (2023). Humidity's role in heat-related health outcomes: A heated debate. *Environmental Health Perspectives*, *131*(5), 055001.

Brown, R. G., & Bretherton, C. S. (1997). A test of the strict quasi-equilibrium theory on long time and space scales. *Journal of the atmospheric sciences*, *54*(5), 624–638.

Buzan, J. R., & Huber, M. (2020). Moist heat stress on a hotter earth. *Annual Review of Earth and Planetary Sciences*, *48*, 623–655.

Byrne, M. P. (2021). Amplified warming of extreme temperatures over tropical land. *Nature Geoscience*, *14*(11), 837–841.

Chiang, J. C., & Sobel, A. H. (2002). Tropical tropospheric temperature variations caused by enso and their influence on the remote tropical climate. *Journal of climate*, *15*(18), 2616–2631.

ECMWF, S. P. (2014). In ifs documentation cy40r1 part iv: Physical processes. *ECMWF: Reading, UK*, 111–113.

Fueglistaler, S. (2019). Observational evidence for two modes of coupling between sea surface temperatures, tropospheric temperature profile, and shortwave cloud radiative effect in the tropics. *Geophysical Research Letters*, *46*(16), 9890–9898.

Gill, A. E. (1980). Some simple solutions for heat-induced tropical circulation. *Quarterly Journal of the Royal Meteorological Society*, *106*(449), 447–462.

Hersbach, H., Bell, B., Berrisford, P., Hirahara, S., Horányi, A., Muñoz-Sabater, J., ... others (2020). The era5 global reanalysis. *Quarterly Journal of the Royal Meteorological Society*, *146*(730), 1999–2049.

Hogikyan, A., Resplandy, L., & Fueglistaler, S. (2022). Cause of the intense tropics-wide tropospheric warming in response to el niño. *Journal of Climate*, *35*(10), 2933–2944.

Ivanovich, C., Anderson, W., Horton, R., Raymond, C., & Sobel, A. (2022). The influence of intraseasonal oscillations on humid heat in the persian gulf and south asia. *Journal of Climate*, *35*(13), 4309–4329.

Klein, S. A., Soden, B. J., & Lau, N.-C. (1999). Remote sea surface temperature variations during enso: Evidence for a tropical atmospheric bridge. *Journal of climate*, *12*(4), 917–932.

Kong, Q., & Huber, M. (2023). Regimes of soil moisture-wet bulb temperature coupling with relevance to moist heat stress. *Journal of Climate*, 1–45.

Lu, Y.-C., & Romps, D. M. (2023). Is a wet-bulb temperature of 35° c the correct threshold for human survivability? *Environmental Research Letters*, *18*(9), 094021.

Matsuno, T. (1966). Quasi-geostrophic motions in the equatorial area. *Journal of the Meteorological Society of Japan. Ser. II*, *44*(1), 25–43.

Pal, J. S., & Eltahir, E. A. (2001). Pathways relating soil moisture conditions to future summer rainfall within a model of the land–atmosphere system. *Journal of Climate*, *14*(6), 1227–1242.

Pan, Y. H., & Oort, A. H. (1983). Global climate variations connected with sea surface temperature anomalies in the eastern equatorial pacific ocean for the 1958–73 period. *Monthly Weather Review*, *111*(6), 1244–1258.

Parkes, B., Buzan, J. R., & Huber, M. (2022). Heat stress in africa under high intensity climate change. *International journal of biometeorology*, *66*(8), 1531–1545.

Raymond, C., Matthews, T., & Horton, R. M. (2020). The emergence of heat and humidity too severe for human tolerance. *Science Advances*, *6*(19), eaaw1838.

Raymond, C., Matthews, T., Horton, R. M., Fischer, E. M., Fueglistaler, S., Ivanovich, C., . . . Zhang, Y. (2021). On the controlling factors for globally extreme humid heat. *Geophysical Research Letters*, *48*(23), e2021GL096082.

Rayner, N., Parker, D. E., Horton, E., Folland, C. K., Alexander, L. V., Rowell, D., . . . Kaplan, A. (2003). Global analyses of sea surface temperature, sea ice, and night marine air temperature since the late nineteenth century. *Journal of Geophysical Research: Atmospheres*, *108*(D14).

Revadekar, J., Kothawale, D., & Rupa Kumar, K. (2009). Role of el niño/la niña in temperature extremes over india. *International Journal of Climatology: A Journal of the Royal Meteorological Society*, *29*(14), 2121–2129.

Rogers, C. D., Ting, M., Li, C., Kornhuber, K., Coffel, E. D., Horton, R. M., . . . Singh, D. (2021). Recent increases in exposure to extreme humid-heat events disproportionately affect populated regions. *Geophysical Research Letters*, *48*(19), e2021GL094183.

Sherwood, S. C., & Huber, M. (2010). An adaptability limit to climate change due to heat stress. *Proceedings of the National Academy of Sciences*, *107*(21), 9552–9555.

Sobel, A. H., Held, I. M., & Bretherton, C. S. (2002). The enso signal in tropical tropospheric temperature. *Journal of climate*, *15*(18), 2702–2706.

Speizer, S., Raymond, C., Ivanovich, C., & Horton, R. M. (2022). Concentrated and intensifying humid heat extremes in the ipcc ar6 regions. *Geophysical Research Letters*, *49*(5), e2021GL097261.

Thirumalai, K., DiNezio, P. N., Okumura, Y., & Deser, C. (2017). Extreme temperatures in southeast asia caused by el niño and worsened by global warming. *Nature communications*, *8*(1), 15531.

Xie, S.-P., Hu, K., Hafner, J., Tokinaga, H., Du, Y., Huang, G., & Sampe, T. (2009). Indian ocean capacitor effect on indo–western pacific climate during the summer following el niño. *Journal of climate*, *22*(3), 730–747.

Yulaeva, E., & Wallace, J. M. (1994). The signature of enso in global temperature and precipitation fields derived from the microwave sounding unit. *Journal of climate*, *7*(11), 1719–1736.

Zhang, Y., & Fueglistaler, S. (2020). How tropical convection couples high moist static energy over land and ocean. *Geophysical Research Letters*, *47*(2), e2019GL086387.

Zhang, Y., Held, I., & Fueglistaler, S. (2021). Projections of tropical heat stress constrained by atmospheric dynamics. *Nature Geoscience*, *14*(3), 133–137.